Relevance of infragravity waves in a wave-dominated inlet

Xavier Bertin, Maitane Olabarrieta

RELEVANCE OF INFRAGRAVITY WAVES IN A WAVE-DOMINATED INLET

Xavier Bertin[1] & Maitane Olabarrieta[2]

[1]UMR 7266 LIENSs, CNRS-Universite de La Rochelle, 2 rue Olympe de Gouges, 17000 La Rochelle, France.
[2]University of Florida, Department of Civil and Coastal Engineering, Gainesville, United States.

E-mail addresses: xbertin@univ-lr.fr (Xavier Bertin); maitane.olabarrieta@essie.ufl.edu (Maitane Olabarrieta)

ABSTRACT

This study investigates the relevance of infragravity (IG) waves at Albufeira Lagoon Inlet, a shallow wave-dominated inlet located on the Western Coast of Portugal. A field experiment carried out in September 2010 revealed the occurrence of low-frequency oscillations (i.e. 25 to 300 s) in water levels and current velocities. While these fluctuations were present over the ebb-tidal delta along the whole tidal cycle, they only appeared between the beginning of the flood and up to two hours after high tide inside the lagoon. The XBeach modeling system was applied to Albufeira Lagoon Inlet and reproduced the generation and propagation of IG waves and their blocking during the ebb. This behavior was explained by blocking due to opposing tidal currents reaching 2.5 $m.s^{-1}$ in shallow water depths. Numerical results suggest that the breakpoint mechanism and the long bound wave shoaling mechanisms contributed significantly to the generation of IG waves in the inlet. IG waves induced fluctuations in flood currents inside the lagoon reaching temporarily 100 % of their magnitude. The fact that these fluctuations occur mostly at flood and not at ebb could promote flood dominance in the lagoon. This hypothesis will have to be verified, namely under storm wave conditions.

KEYWORDS
Infragravity waves, wave-dominated inlet, low frequency waves, wave blocking.

Keypoints
- Measurements revealed energetic IG waves in a wave-dominated inlet.
- Breakpoint generation and bound-wave shoaling both contributed significantly to IG wave generation.
- IG waves were blocked by opposing ebb-currents.

1. INTRODUCTION
Tidal inlets are transition zones between the ocean and back-barrier lagoons or estuaries where constant exchange of water, sediments, nutrients and larvae occurs. Hydrodynamics and morphological changes in tidal inlets have strong ecological and socio-economic repercussions, since they affect navigation safety, flooding extent, erosion of adjacent beaches, water renewal and material exchange between the lagoon (orestuary) and the open ocean. Due to the complex interactions between tides, wind waves, river outflows, sediments transport and morphology, understanding the resulting hydrodynamics and sediment transport patterns is still a challenge.

47 Nonetheless, an increased knowledge of these processes is needed to improve the management
48 and maximize the resilience of these coastal systems.
49
50 In the last decade several studies (e.g. Siegle et al., 2004; Bertin et al., 2009; Olabarrieta et al.,
51 2011; Dodet et al., 2013; Orescanin et al., 2014; Wargula et al., 2014; Olabarrieta et al., 2014,
52 Chen et al., 2015) have emphasized the relevance of surf-zone processes in mixed-energy and
53 wave-dominated tidal inlets. Shallow water depths over the ebb-tidal delta can induce wave
54 breaking and subsequent surf-zone circulations. Wave-breaking accelerations can also affect the
55 extension and direction of ebb currents, as well as impact the hydrodynamics inside the estuary.
56 For example, wave breaking over the ebb-tidal delta can induce a wave setup and increase water
57 levels at the scale of the whole lagoon or estuary (e.g. Malhadas et al. 2009; Bertin et al., 2009;
58 Olabarrieta et al., 2011; Dodet et al. 2013; Arnaud and Bertin, 2014; Bertin et al., 2015).
59 Moreover, due to the interaction between the wave bottom boundary layer and tidal currents,
60 bottom friction increases (e.g. Grant and Madsen 1979, Soulsby et al., 1997) and,consequently,
61 can affect the overall tidal propagation (Olabarrieta et al., 2011 and Dodet et al., 2013).
62
63 The relevance of oceanic infragravity waves (hereafter, "IG waves") in the nearshore is well
64 recognized and many studies have been conducted in the last four decades to ascertain their role
65 in coastal morphodynamics (e.g. Guza et al., 1984; Masselink, 1995; Baldock and Huntley,
66 2002; Baldock et al., 2004; Pomeroy et al., 2012). IG waves are ocean waves with periods from
67 25 to more than 300 seconds associated with the presence of groups in gravity waves. To date,
68 two main mechanisms for the generation of infragravity waves have been proposed. Longuet-
69 Higgins and Stewart (1964) suggested that the observed free infragravity wave or "surf beat"
70 may be due to the shoaling, release and subsequent reflection of bound long waves after the
71 gravity waves break in the surf-zone. Bound waves result from 2nd-order non-linear wave-wave
72 interactions between wind waves ("forced" IG waves: [Hasselmann, 1962; Longuet-Higgins and
73 Stewart, 1962; Okihiro et al., 1996]). An alternative mechanism for the generation of surf beat
74 was presented by Symonds et al. (1982) and Schäffer (1993), who considered the temporal
75 variation of the breakpoint as a wave maker, generating surf beat both seaward and shoreward.
76 The moving breakpoint mechanism can also be thought as a "dynamic set-up" in the surf-zone.
77 Large waves break earlier and produce larger set-up than small waves in the wave group, which
78 introduces oscillations in the set-up at the group frequency. The first mechanism was shown to
79 be dominant on gently sloping beaches due to the shoaling of the bound-wave (e.g. List 1992;
80 Herbers et al., 1995; Pomeroy et al., 2012) while the second mechanism occurs preferably when
81 gravity waves break within a narrow zone, which condition is preferentially met over a steep
82 bottom (Battjes et al, 2004; Van Dongeren et al., 2007; Baldock, 2012; Pomeroy et al., 2012).
83
84 Despite being known that mixed-energy and wave-dominated tidal inlets share characteristics of
85 beach and tidally dominated areas (e.g. Siegle et al., 2004; Bertin et al., 2009; Olabarrieta et al.,
86 2011), the dynamics and effects of IG waves in tidal inlets have not yet been addressed
87 according to the author's knowledge IG wave generation, propagation, and dissipation
88 mechanisms in tidal inlets might differ substantially from those observed in beach environments
89 for several reasons. First, the inlet morphology, characterized by the presence of an ebb-tidal
90 delta, a main channel and secondary channels, is usually more complex than a beach
91 morphology. Moreover, ebb-tidal deltas combine gentle slopes in their central part and steep
92 slopes in their terminal lobes so that both generation mechanisms for IG waves can be active

93   along a tidal cycle. Second, while in a beach all incoming IG wave energy is dissipated or
94   reflected, in a tidal inlet part of the IG energy might, depending on the tidal phase, propagate
95   through the main channel and into the inner part of the lagoon or estuary. Finally, IG waves in
96   tidal inlets can be affected by strong flood and ebb currents.
97
98   Different types of approaches and numerical models have been considered to numerically model
99   the generation and propagation of infragravity waves. Two main approaches or types of models
100   can be distinguished: 1) phase-resolving (e.g, Herbers et al. 1995; Madsen et al., 1997; Kennedy
101   et al., 2000; Torres- Freyermuth et al., 2010; Bonneton et al., 2011; Zijlema et al., 2011Ma et al.,
102   2012; Ruju et al., 2012; Rijnsdorp et al., 2015; Sheremet et al., 2016) and 2) phase-averaged
103   models (e.g. Reniers et al. 2004, 2006, 2010; Uchiyama and McWilliams, 2008; Long and
104   Haller, 2009; Roelvink et al., 2009, Eldeberky et al., 2015). Phase-resolving models account for
105   the non-linear gravity wave transformations and possible non-linear energy transfer from the IG
106   band to the gravity band. Because of the high computational cost, the application of phase-
107   resolving models is limited to areas of hundreds of meters and time periods shorter than a tidal
108   cycle. On the other hand, coupled models are computationally more efficient, but they disregard
109   the aforementioned non-linear processes.
110
111   This study is focused on the Albufeira Lagoon Inlet located on the western coast of Portugal.
112   This wave-dominated inlet closes seasonally in autumn/early winter, usually after energetic swell
113   conditions. Dodet (2013) simulated its morphodynamic evolution under tides and gravity waves
114   and, although the fast morphological changes of the inlet were in overall well captured, its
115   closure was not reproduced, as if one or several relevant processes were not accounted for in
116   these simulations. This study tackles, for the first time, the role of infragravity waves on the
117   hydrodynamics in a wave-dominated inlet. In particular, attention is given to the main IG wave
118   generation mechanisms andto their interactions with tides. Possible impacts of these long waves
119   in sediment transport and morphodynamics are also discussed.
120
121   The paper is organized as follows. A brief description of the study area is provided in Section 2.
122   The methods, including the data acquisition and post-processing, as well as the numerical model,
123   are described in Section 3. Observed and modeled tides, gravity and IG waves are described and
124   compared in Section 4. Model limitations, IG wave generation and propagation mechanisms, and
125   implications on sediment transport and morphodynamics are discussed in Section 5. The main
126   conclusions are summarized in Section 6.
127

128   **2. STUDY AREA**
129   Albufeira Lagoon is located on the Western coast of Portugal, about 20 km South of Lisbon. The
130   width of the continental shelf in front of the inlet is limited to 5 km due to the Lisbon Canyon
131   (Figure 1A). The lagoon covers an elongated surface area of 1.3 km^2 SW-NE orientated and is
132   connected to the sea through a small and shallow intermittent inlet. The inlet exhibits a strong
133   seasonal behavior, leading to its natural closure in autumn/early winter, after which it is
134   artificially opened in spring (Dodet et al., 2013; Fortunato et al., 2014). The inlet is bordered by
135   steep beaches (slope of the order of 0.10) made of coarse sands (d_{50} = 0.0007-0.0018 m).
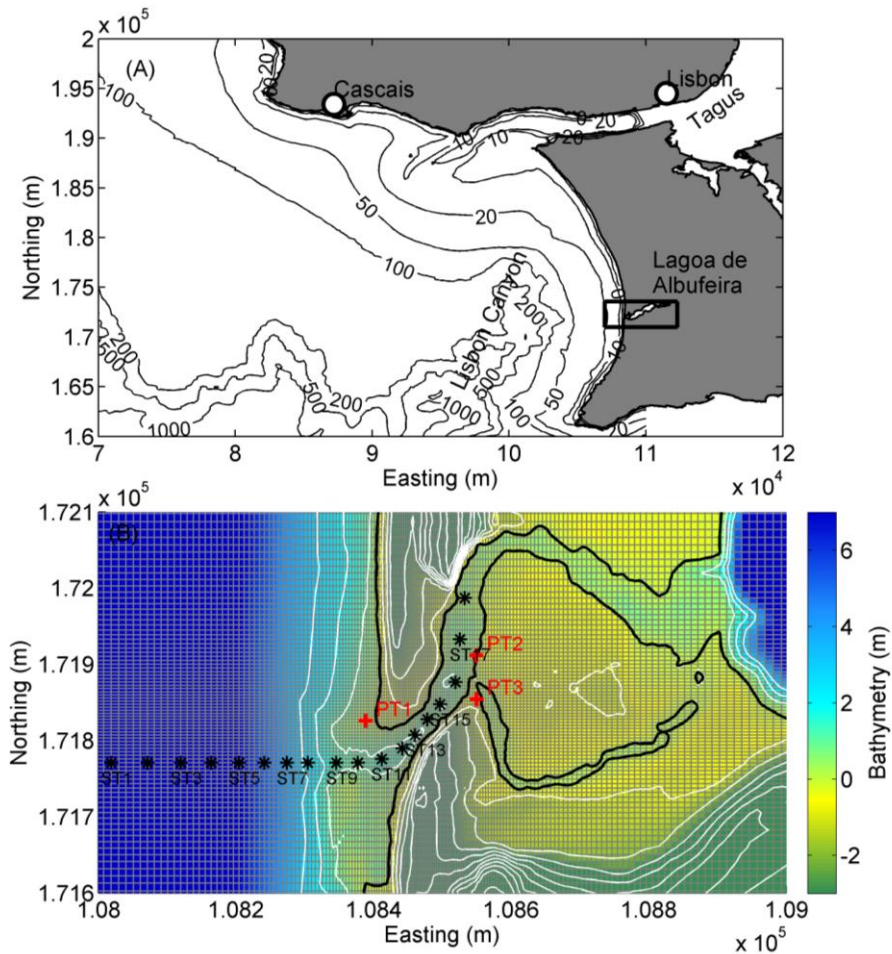
136
137 Figure1. (A) Regional bathymetry of the study area and (B) Detailed bathymetric map of
138 Albufeira Lagoon Inlet, computational grid used for XBeach (grey frame), location of the
139 pressure sensors (red crosses), model stations (black stars). At PT2 current velocities where also
140 measured with an electromagnetic current-meter. The black solid line corresponds to mean
141 sea-level contour line. The bathymetric map of the Albufeira Lagoon Inlet shown in panel B
142 does not represent the whole computational domain. The model grid covers the whole lagoon.

143 This area is subjected to semi-diurnal tides, the amplitude of which ranges from less than 1 m to
144 more than 3.5 m. The mean tidal prism during spring tides is of the order of $80 \cdot 10^4$ m^3 (based on
145 the numerical estimates of Fortunato et al., 2014). Tides are strongly distorted throughout their
146 propagation across the inlet, semi-diurnal tidal constituents are severely damped while quarter-
147 diurnal and fortnightly non-linear constituents develop. Inside the lagoon, the amplitude of the
148 semi-diurnal constituents experiences a seasonal cycle, with a maximum in late summer after
149 which it decreases until the lagoon closes. This behavior is commonly observed at other
150 Portuguese shallow inlets and was explained by the shoaling of the inlet due to several wave-
151 induced processes (Bertin et al., 2009; Dodet et al., 2013).
152
153 The study area is exposed to an energetic wave climate, particularly in winter. Based on a 57-
154 year wave numerical hindcast (Dodet et al., 2010), the mean annual deep water (10.0ºW; 38.0ºN;
155 ~ 3000 m deep) significant wave height (H_{m0}), mean direction (MWD) and peak period (T_p) are

156 respectively 1.9 m, 312 °, and 10.5 s. During winter (resp. summer) the corresponding values are:
157 2.5 m, 305 °, and 12.1 s (resp. 1.3 m, 319° and 8.4 s). The drainage basin of the Albufeira Lagoon
158 covers a surface area of around 106 km^2, but the freshwater discharge is only significant under
159 heavy rain, which usually occurs when the lagoon is closed.
160
161 **3. METHODS**
162 IG wave dynamics and their relevance in Albufeira Lagoon are analyzed combining field
163 measurement analysis and numerical modelling. Water levels and currents were measured in the
164 field experiment described by Dodet et al. (2013). The experiment was not specifically designed
165 to study IG waves, and, therefore, the location of the instruments prevents the understanding of
166 the main generation and propagation mechanisms from the data analysis. To complement the
167 analysis and ascertain the main IG wave generation and propagation mechanisms, we applied the
168 modeling system XBeach (Roelvink et al., 2009), version 1.21.3866M, 'Groundhog Day'
169 release.
170
171 ***3.1 Field measurements***

172 During the Albufeira Lagoon Inlet field experiment, water levels and currents were measured on
173 the ebb-tidal delta (PT1), on the flood-tidal delta (PT2) and at the tip of the sand-spit (PT3)
174 located on the southern margin (Figure 1B). A high-resolution Acoustic Doppler Current Profiler
175 (ADCP) was collocated at PT1, while and electromagnetic current-meter was collocated at PT2.
176 Pressure measurements were first corrected from the atmospheric pressure variations. The entire
177 record was split into consecutive bursts of 30 minutes and the bursts in which the sensor was
178 alternatively dry were not considered. Bottom pressure energy density spectra *Ep(f)* were
179 computed using Fast Fourier Transform, with 2 Hanning-windowed segments (32 degrees of
180 freedom). Considering that the spectral integrals are Chi-square distributed, confidence intervals
181 (hereafter CI) for a given level α were computed according to Bendat and Piersol (1971):
182

183 $$CI = \left[\frac{v}{\chi^2_{v,1-\alpha/2}} ; \frac{v}{\chi^2_{v,\alpha/2}} \right]$$

184
185 These pressure spectra were then converted into elevation spectra *E(f)* considering the linear
186 wave theory. The significant wave height (*H$_{m0}$*) was computed as:
187
188 $H_{m0} = 4\sqrt{m_0}$ (1)

189 Where,

190 $m_0 = \int\limits_{f_{\min}}^{f_{\max}} E(f)\, \partial f$ (2)

191 Where *f$_{min}$* and *f$_{max}$* were set to 0.04 and 0.5 Hz for the gravity band and 0.002 and 0.04 *Hz* for
192 the infragravity band, respectively.
193

194 ### *3.2 Numerical model*

195 XBeach is a two-dimensional modelling system that couples the St. Venant equations with a
196 simplified wave-action conservation model, a sediment transport and bed update model. To
197 simulate the generation and propagation of IG waves, XBeach can be forced with time varying
198 directional wave spectra defined at the boundaries. Since the wave spectra do not contain the
199 phase information, the model assumes random phases and applies a single summation technique
200 to reconstruct the free surface elevation time series at the boundaries. A Hilbert transform is
201 applied to derive time series of the gravity wave energy (that varies at the wave group scale) and
202 these are imposed as boundary conditions for the wave-action balance equation. The incoming
203 bound-wave is computed following Herbers et al. (1994), and is imposed along the open
204 boundary of the flow model.

205
206 In this study, depth-induced wave breaking energy dissipation was computed using the
207 parameterization proposed by Daly et al. (2012). Wave-current interactions are also considered
208 in the model. The interaction between currents and gravity waves is included in the gravity wave
209 dispersion relation modified by the Doppler Effect and in the eikonal equation. Dissipation of
210 gravity waves by whitecapping induced by opposing current is not considered. The dynamics of
211 IG waves, including their generation and propagation, are implicitly considered by the St. Venant
212 equations. Therefore, the effects of currents on IG wave propagation, including their possible
213 blocking, are represented by the equations and do not need to be explicitly included. The reader
214 is referred to Roelvink et al. (2009) for a detailed description of XBeach.

215
216 A rectilinear grid (with variable grid size) covering the whole lagoon and extending to offshore
217 water depths of 20 m was implemented. The spatial resolution ranged from 20 m along the open
218 boundary to 3 m at the inlet (Fig. 1B). Such a fine resolution was required to adequately
219 represent the inlet channel and resulted in a 210 by 380 nodes grid. Along the open boundaries,
220 XBeach was forced with time-series of water levels recorded at the nearby Cascais tide gauge
221 (Fig 1A) and the time varying directional wave-spectra originated from an application of SWAN
222 (Booij et al., 1999) at the scale of the Cascais Bay as described in Dodet et al. (2013). This
223 SWAN run was forced along its open boundaries with time series of wave energy spectra
224 computed from an application of the WaveWatchIII model (Tolman, 2009) at the scale of the
225 Atlantic Ocean (Crawford et al., 2015) and forced with wind fields originating from the ERA-
226 INTERIM reanalysis (Dee et al., 2011).

227
228 Bottom friction was represented by a non-linear quadratic bottom shear stress with a constant
229 Chezy coefficient (equal to 30 $m^{0.5}.s^{-1}$). The horizontal eddy viscosity was assumed constant (0.5
230 m^2/s). The minimum water depth was set to 0.2 m and 0.25 m for the computation of the Stokes
231 velocities. The breaking parameter γ was set to 0.4 and γ_2 to 0.3. These values provided the best
232 agreement between measured and modeled free-surface elevations and velocity magnitudes.

233
234 The model was run for the duration of the field experiment (2 days), and time series of surface
235 elevation, current velocities were archived at a 5 s interval. Spectral estimates were computed
236 following the same methodology as for the field observations (section 3.1). To analyze the IG
237 wave generation mechanisms and their relevance different simulations were run (Table1). In all
238 of them tidal propagation was taken into account. Run 0 did not consider gravity waves, only
239 tides. Run 1, considered tides and gravity waves but wave groups were not taken into account.

240 Run 2 included the effect of tides, gravity waves and wave groups. Run 3 is the same
241 configuration as Run 2 (considers the same random phases to reconstruct the wave envelope
242 signal) but wave forces were turned off when the gravity waves were breaking. In Run 4, wave
243 forces were turned off outside the surf-zone and the incoming bound wave at the boundaries
244 were turned off, so that only the wave breaking variation at the scale of the wave groups
245 contributes to the IG wave generation. Run 5 did not include any wave forces and it only
246 propagated the tide and the incoming bound wave defined at the boundaries. Runs 3 to 5 were
247 designed to analyze the relative contribution of the different IG wave generation mechanisms. To
248 ensure that runs 1 to 5 had the same model setting, we first ran Run2 and we stored the wave-
249 group changing energy and flux boundary conditions. These were directly used in runs 3 to 5.
250 Since Run1 did not account for the gravity energy modulation, the previously stored energy
251 boundary condition was low-pass filtered and imposed in Run 1. For model/measurement
252 comparison shown in section 4, 7 more simulations (Run 6 to 12) were done considering tides,
253 gravity and IG waves (same configuration as run 2). The ensemble-mean of these realizations
254 was used for the model verification.

255
256

	Run0	Run1	Run2	Run3	Run4	Run5	Runs 6-12
Tides	Yes	Yes	Yes	Yes	Yes	Yes	Yes
Gravity waves	No	Yes	Yes	Yes	Yes	No	Yes
IG waves	No	No	Yes	Yes	Yes	No	Yes
Radiation stress inside surf-zone	No	Yes	Yes	No	Yes	No	Yes
Radiation stress outside surf-zone	No	Yes	Yes	Yes	No	No	Yes
Bound wave at offshore boundary	No	No	Yes	Yes	No	Yes	Yes

257 Table 1. Characteristics of the numerical simulations.

258
259 4. RESULTS
260 Tidal and gravity wave characteristics during the field experiment are described by Dodet et al.
261 (2013) and will not be the main focus of this section. However, since gravity waves and IG wave
262 propagation and generation can be affected by water levels and tidal currents model results are
263 going to be dependent on how well water levels and currents are reproduced by the model.
264 Therefore, it is necessary to verify modeled water levels and currents and to show the
265 comparison between modeled and measured tidal and gravity waves for a correct interpretation
266 of the results.

267
268 4.1 *Tidal propagation across the inlet*

269 The field experiment covered 3 tidal cycles and took place during spring tide conditions (Figure
270 2). The mean tidal range was 2.45 m, with a minimum of 2.31 m and a maximum of 2.54 m. The
271 tidal wave offshore the Albufeira Lagoon is symmetric, but the non-linear tidal propagation
272 through the inlet produces significant distortion (see Figure 3.a). As a consequence, the tidal
273 range inside the lagoon was reduced by more than 50% compared to the ocean. As usually

274 observed in friction-dominated tidal inlets, the mean water level inside the lagoon increased
275 compared to the ocean, although mean water levels inside the lagoon were also affected by wave
276 induced forces (Dodet et al., 2013). In overall, tidal propagation was well reproduced with the
277 numerical model as reflected in the model skill values (see Table 2).
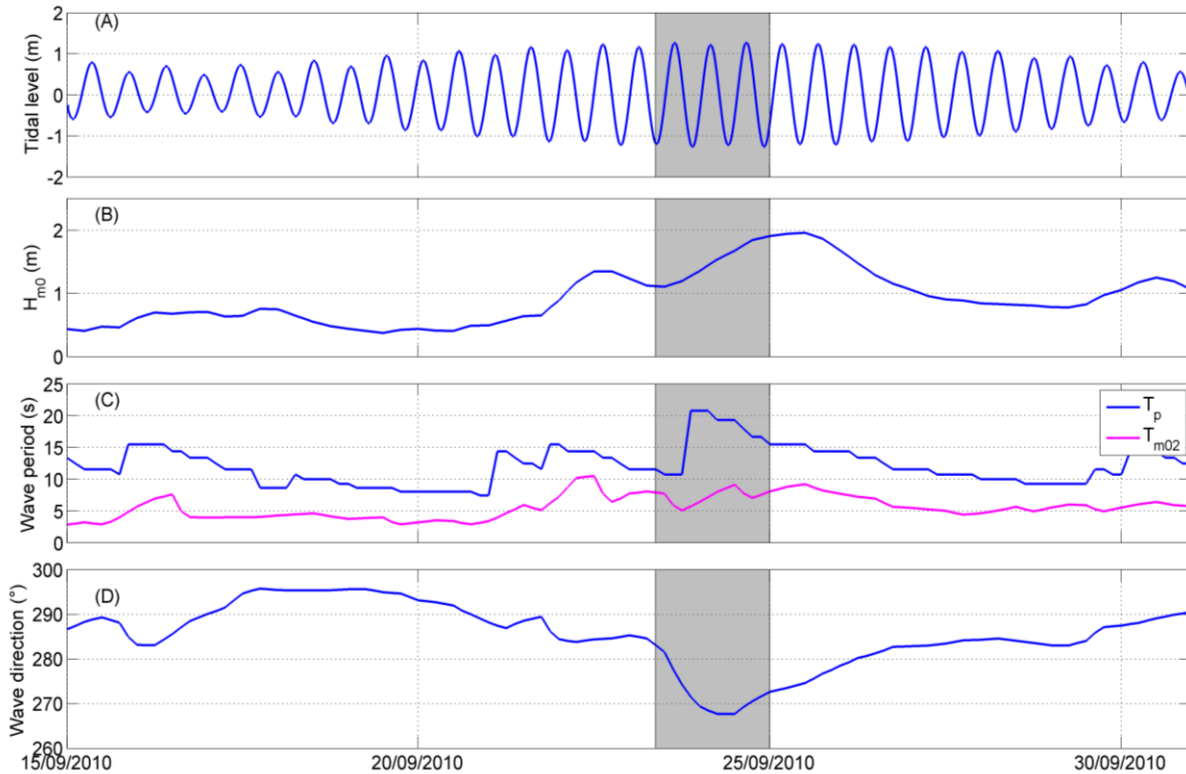
278

279 Figure 2. Offshore hydrodynamic conditions during the 15th and 31st of September 2010, (A)
280 tidal level measured at the tidal gauge nearby Cascais, (B) deep water significant wave height,
281 (C) deep water wave periods, and (D) deep water mean wave direction. Deep water wind wave
282 characteristics were computed with Swan model, offshore the inlet at a water depth of 100 m.
283 The shadowed area represents the period of the field experiment.

284 The Root Mean Square Error (RMSE) between modeled and measured water level variations at
285 the ebb-tidal delta station (PT1) was 0.07 m, at PT12 0.08 m and 0.06 m at PT3. These values
286 were still smaller than 10% of the tidal range at each station, which indicates that the model
287 reproduced adequately the tidal distortion as its propagation through the inlet and inner lagoon.

288
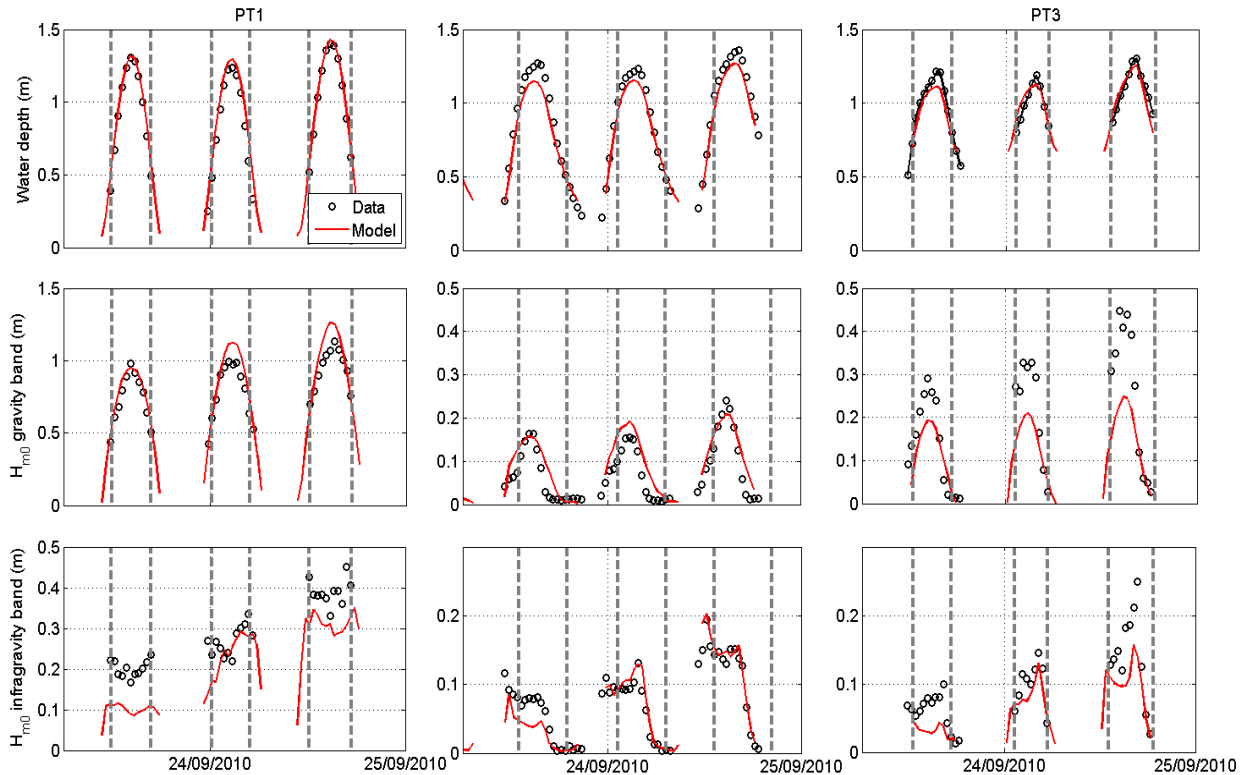
Figure 3. Measurement (black circles) and model result for Run2 (red curve) comparison at the three measurement stations. Top panels show the low-pass filtered (*f*<0.002 Hz) free surface elevation time series, middle panels $H_{m0,G}$ time series and bottom panels $H_{m0,IG}$ time series. The grey dashed vertical lines indicate a similar water level at ebb and flood and help identifying large differences in short and IG waves between ebb and flood. Model results represent the ensemble-mean of 8numerical simulations, statistically equivalent to Run2.

Currents were also measured at PT2 by means of an electromagnetic current meter, located 0.4 m above the bed. The comparison with modeled currents averaged over 30 minute samples at this sensor reveals a fair agreement, with a RMSE of 0.10 m/s and only a slight underestimation of the flood peak, leading to a -0.05 m/s negative bias (Figure 4) and a 0.98 Willmott Skill Score (WSS) (Table 3). However, since this sensor was located on the ramp of the flood-delta (Figure 1), it was sheltered from ebb currents. In the main channel (ST 13) modeled ebb currents were twice as strong as flood currents and temporarily reached 2.5 m/s (Figure 4).

302
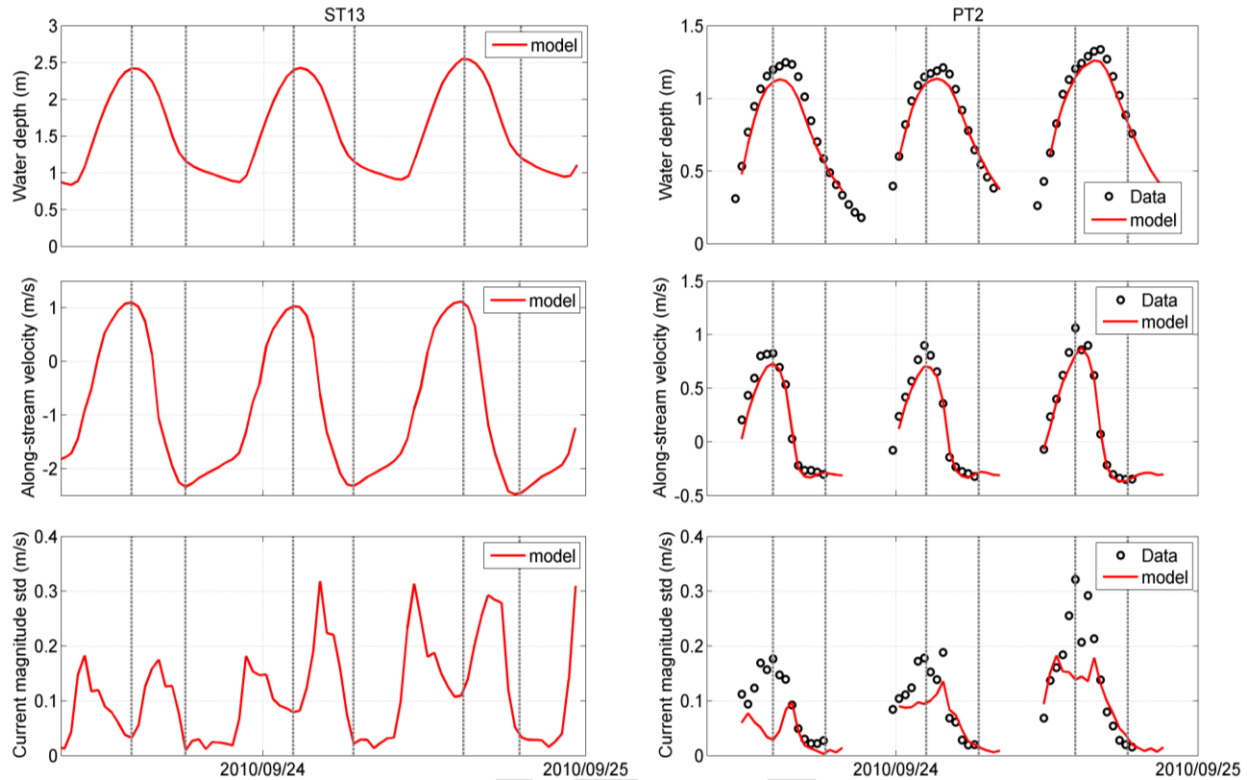
Figure 4. Modeled (red) against measured (black circles) water depth (top row), along-stream current velocity (middle row) and standard deviation of the current magnitude computed over 30 minute samples (bottom row) in the inlet main channel (ST13, Figure 1) and at PT2. The grey dashed lines indicate the time where maximum flood and ebb currents occurred. The standard deviation of the current magnitude computed over 30 minute samples has been previously low-pass filtered with a 25 s window to remove orbital motions of gravity waves.

4.2 Characterization of gravity waves

Deep-water gravity wave energy and the peak period (T_p) increased during the field experiment (Fig2). The 23rd of September T_p was 12.5 s and the significant wave height ($H_{m0,G}$) 1 m. At the end of the experiment swell waves propagating from the west hit the inlet, and consequently T_p and $H_{m0,G}$ increased to more than 20 s and 1.8 m respectively.

In all the stations, gravity waves were depth limited and, therefore, tidally modulated (Figure 3). Maximum $H_{m0,G}$ were observed during high tide at PT1, especially in the last tidal cycle, when values over 1.2 m were measured. This station became dry from mid to low tide. At PT1 the model RMSE was 0.09 m (see Table 2), and the tidal modulation was well captured. The Willmott Skill Score (defined in Appendix A) was larger than 0.92 at PT1 and PT2, and decreased to 0.76 at PT3, mostly due to a negative bias.

Gravity waves damped when propagating from the ebb-delta to the inner lagoon (Figure 3). $H_{m0,G}$ decreased from PT1 on average ~91% at PT2 and ~76% at PT3 during high tide. Modeled

323 $H_{m0,G}$ mean reductions were ~86% at PT2 and ~84% at PT3. The highest RMSE (~0.10 m) was
324 obtained at PT3, where the model underestimated $H_{m0,G}$, especially during the last high tide.

325 During the ebb, $H_{m0,G}$ at PT2 decreased sharply and at mid-ebb $H_{m0,G}$ was lower than 0.025 m
326 (Figure 3). This fast reduction after the beginning of the ebb up to low tide was already explained
327 by wave blocking at the inlet (Dodet et al., 2013). The $H_{m0,G}$ tidal modulation observed in the
328 measurements was well reproduced with the numerical model. However, the blocking during the
329 mid-ebb was underestimated by the model.

4.3 Characterization of IG waves

331 Measurements revealed the occurrence of low frequency oscillations (i.e. 25 to 300 s) in the ebb-
332 delta (PT1) and interior stations (PT2 and PT3). During the experiment, IG wave significant
333 wave height ($H_{m0,IG}$) increased from 0.2 m to more than 0.5 m at the ebb-tidal delta (PT1). The
334 largest $H_{m0,IG}$ was observed during the last tidal cycle of the 24th of September, when offshore
335 wind waves where most energetic and the period was largest (see Figure 2). This swell originated
336 from a remote storm (Dodet et al., 2013).

337 Mirroring the behavior of the gravity band, IG waves were tidally modulated and $H_{m0,IG}$
338 decreased from the ebb-tidal delta (PT1) to the inner part of the lagoon (Figure 3). Due to the
339 shallow water levels at PT1, the station became dry during half of the tidal cycle. In the three
340 tidal cycles covered by the experiments, two local maxima of $H_{m0,IG}$ could be identified at PT1,
341 the first before and the second after high tide. Between these two local maxima, specifically
342 during high tide, a local minimum of $H_{m0,IG}$ was observed.

343 At PT2 and PT3, the observed tidal modulation was not related to the drying of the stations,
344 since they only became dry at the lowest tidal levels. After mid-ebb, IG wave energy levels at the
345 inner stations were very low ($H_{m0,IG}$ decreased by more than 90% with respect to the maximum
346 values observed during each tidal cycle), suggesting a possible blocking of IG waves. As an
347 example, Figure 6 depicts the water elevation measurements at PT2. The water elevation time
348 series, showed fluctuations both in the gravity and IG bands, especially during late flood, high
349 tide and at the begin of the ebb. After high tide, as the water elevation decreased, $H_{m0,G}$ and
350 $H_{m0,IG}$ decreased drastically. $H_{mo,G}$ reduction occurred on average 20-25 minutes before the
351 decrease of the IG band.

352 XBeach captured both the IG wave energy decrease from the ebb-tidal delta to the inner part of
353 the lagoon and the tidal modulation (see Table 2). At PT1 the model tended to underestimate the
354 observed IG wave energy levels, particularly during the first tidal cycle (RMSE=0.08 m), while
355 at PT2 and PT3 $H_{m0,IG}$, model results were closer to the measurements (RMSE=0.02 and 0.04 m
356 at PT2 and PT3 respectively). As indicated by the Willmott Skill Score the model performance
357 was good in all the stations. As observed in the measurements, model results showed an increase
358 of the $H_{m0,IG}$ just before and after the high tide, with a local minimum at high tide. Although this
359 tendency was observed in all the stations, it was more pronounced at PT3, especially during the
360 last tidal cycle. As observed in the measurements, modeled IG waves almost disappeared after
361 mid-ebb at PT2 and PT3.

362   In addition to bulk parameters, measured and modeled frequency distributions of the energy
363   associated with IG waves were also compared during the flood (T1) and during the ebb periods
364   of the second tidal cycle (Figure 5). At PT1, the frequency distribution of the IG wave energy
365   was well captured by the model, although the energy level of the gravity band was
366   underestimated by the model. In particular, the maximum of energy was found in the same
367   frequency band in the model and in the measurements (0.02-0.04 Hz). The wave spectrum during
368   flood and ebb did not change significantly. Inside the lagoon (PT2 and PT3), the frequency
369   repartition of energy was also well captured by the model during the flood, particularly at PT2,
370   which mirrors the good agreement between model and data for $H_{m0,IG}$ (Figure 3). During the ebb,
371   the two orders of magnitude drop of energy at the highest frequencies was well captured by the
372   model, particularly at PT2.
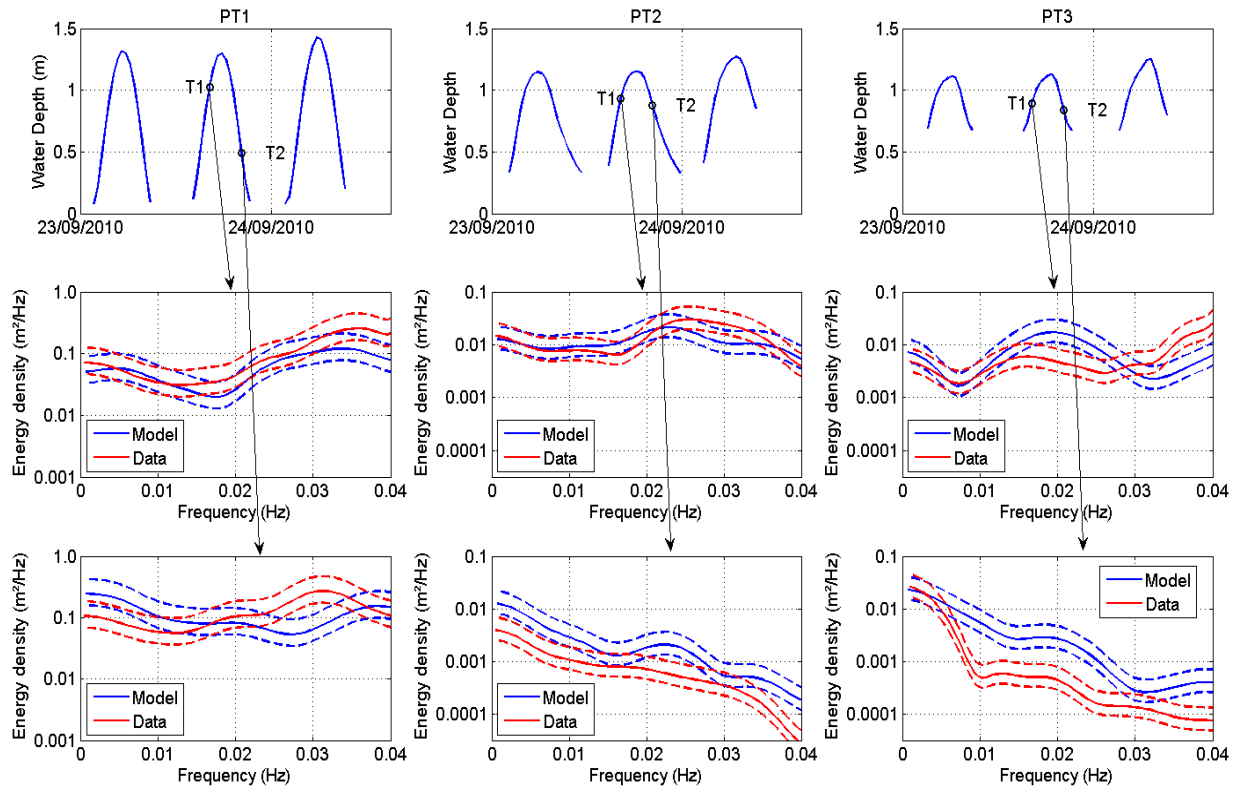
373

374   Figure 5. Water depth (top row), IG wave energy density spectra of energy at T1 (middle row)
375   and IG wave energy density spectra of energy at T2 (bottom row) at PT1 (left column), PT2
376   (middle column) and PT3 (right column). Measured and modeled spectra are depicted in red
377   and blue respectively. Dotted lines represent the 95% confidence interval of the spectra.

378

379   Low frequency fluctuations in the range 25 to 300 s were also observed in the currents velocities
380   recorded at PT2 (Figure 4). The largest current fluctuations in the infragravity band occurred
381   nearly in phase with maximum flood currents and rapidly dropped after the beginning of the ebb.
382   After mid-ebb, these current fluctuations were almost inexistent. XBeach captured reasonably
383   the time evolution of these velocity fluctuations, although with a substantial underestimation of
384   the peak (Figure 4).
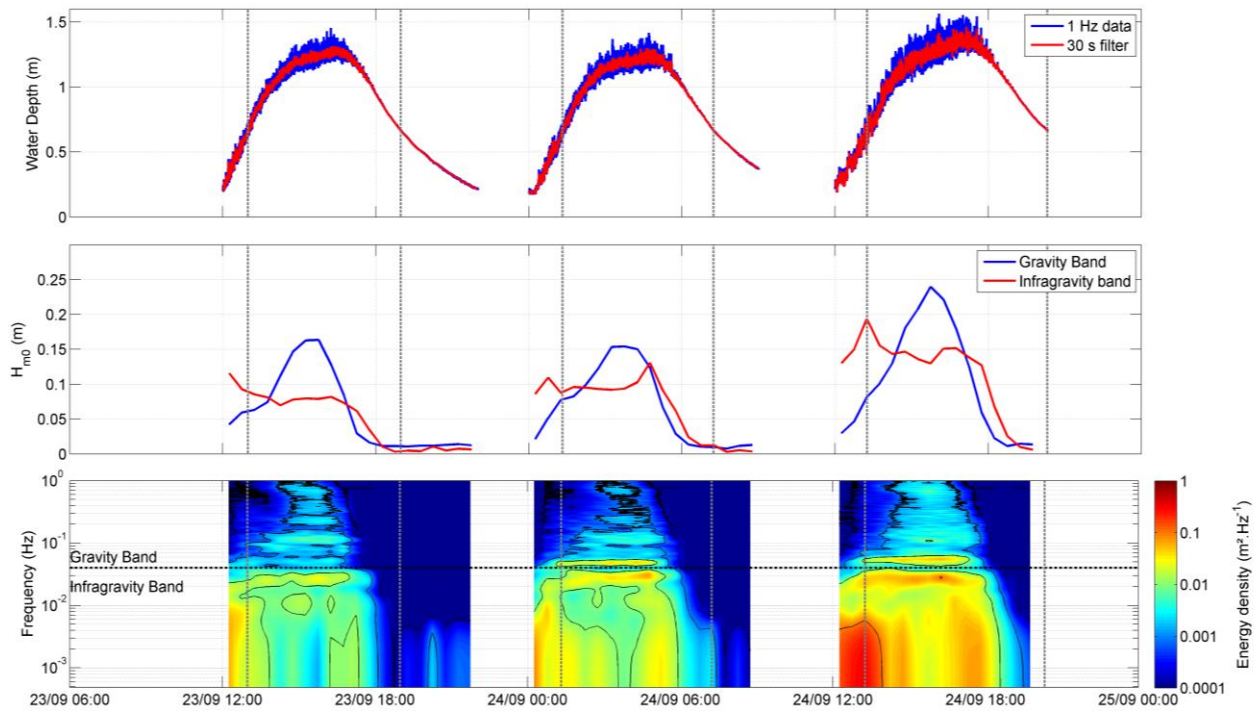
385

386 Figure 6. Time series of the measured free surface elevation (top), $H_{m0,G}$ and $H_{m0,IG}$ (middle), and
387 frequency repartition of energy density (bottom) at PT2.

	Free surface elevation (tides+ wave setup)				$H_{m0,G}$					$H_{m0,IG}$		
	RMSE (m)	NRMSE (%)	BIAS (m)	WSS	RMSE (m)	NRMSE(%)	BIAS (m)	WSS	RMSE (m)	NRMSE (%)	BIAS (m)	WSS
PT1	0.07	6.7	0.06	0.98	0.09	11	0.07	0.95	0.08	28	-0.07	0.79
PT2	0.08	8.5	-0.06	0.98	0.03	44	0.02	0.92	0.02	24	-0.004	0.96
PT3	0.06	6	-0.03	0.94	0.1	48	-0.07	0.76	0.04	41	-0.03	0.805

388 Table 2 Root Mean Square Error (RMSE), Normalized Root Mean Square Error (NRMSE), bias
389 and model skill (Willmott Skill Score, WSS) for free surface elevation (tides+ wave setup),
390 $H_{m0,G}$ and $H_{m0,IG}$. For a perfect model that reproduces the observation exactly, the WSS is one.

391

	RMSE (m/s)	Bias (m/s)	NRMSE (%)	WSS (-)
Along-stream current magnitude	0.10	-0.05	21	0.98
Current magnitude standard deviation	0.07	-0.04	53	0.76

392

393 Table 3 Root Mean Square Error (RMSE), bias, Normalized RMSE and model skill (Willmott Skill
394 Score, WSS) for current magnitude and standard deviation.

395

5. DISCUSSION

This section points out the limitations of the considered modeling approach, and describes the main mechanisms that trigger IG waves in Albufeira Lagoon and the propagation processes along the tidal inlet. In the absence of water level measurements outside the surf-zone, it was not possible to analyze the dominant IG wave generation mechanism based on the observations. Considering that XBeach reproduced IG energy evolution reasonably both inside and outside the lagoon, we used model results alternatively. The section also discusses the possible implications of IG waves on sediment transport and morphodynamics in wave-dominated inlets.

5.1 Limitations of the modeling approach

The comparison between modeled and measured water levels showed a good agreement, with RMSE lower than 0.1 m. Wave heights in the gravity band ($H_{m0,G}$) were also reasonably reproduced, with RMSE ranging from 0.04 to 0.10 m. On the ebb-tidal delta $H_{m0,G}$ were slightly overestimated at high tide. This problem was also pointed out by Dodet et al. (2013) and explained by limitations in the available bathymetric data. Inside the lagoon, the model overestimated wave heights at the beginning of the ebb, although the total blocking that occurred after mid-ebb was well captured. The fast drop of wave height at the beginning of the ebb was explained by Dodet et al. (2013) by an increase in wave steepness due to strong opposing currents, which induces dissipation by whitecapping. The increase in wave steepness is due to shoaling induced by opposing currents. This hypothesis was corroborated by time series of wave energy spectra (Figure 6), which shows that the highest frequencies were dissipated first. Since XBeach considers a single frequency in the gravity band, this process cannot be accurately represented, and could explain the overestimation of wave height at the beginning of the ebb. The under prediction of $H_{m0,G}$ at PT3 and over prediction at PT2 during the flood and high tide could also be due to the fact that we are not considering any diffraction effects.

$H_{m0,IG}$ time series were reasonably reproduced, with RMSE of the order 0.02 to 0.08 m. In particular, $H_{m0,IG}$ were underestimated by up to 25%, and even 50% at the first tidal cycle at PT1 (Figure 3). Among the different possible reasons, the fact that IG and gravity waves are represented in different models doesn't allow a proper representation of all the non-linear interactions that can affect the generation, propagation and dissipation of IG waves. For instance, the merging of bores in the surf-zone (e.g. Senechal et al., 2001; van Dongeren et al., 2007) cannot be represented in such modeling approach, which would lead to an overestimation of energy in the gravity band and an underestimation in the IG band, as observed here. These model limitations, together with the limitations in the available bathymetric data could explain why at PT1 the WSS indicates a lower model performance. This underestimation of IG waves can also explain the underestimation of low frequency fluctuations in the currents observed at PT2 (Figure 4). In addition, the relationship between $H_{m0,IG}$ at the entrance of the lagoon and the magnitude of the current fluctuation inside the lagoon doesn't appear to be linear. This non-linearity could be related with the rapidly changing bathymetry around the flood delta but this hypothesis will have to be verified in future studies.

However, despite these limitations, the low RMSE and acceptable model skills values would suggest that XBeach captures the main processes responsible for IG wave generation and propagation during the experiment. Therefore, the following points of the discussion rely on

439 numeric results and experiments, intended to better understand the relevance of IG waves on
440 tidal inlet dynamics.
441

5.2 IG wave generation

443 With the free surface elevation stored at each computational node with a 5 s interval, for each
444 model simulation, the time variation of the IG energy variance was computed every 10 minutes.
445 The energy variance evolution, through a transect that extended from offshore of the inlet (at
446 water depths of 10 m), along the main channel, to the interior part of the lagoon, was analyzed
447 and compared between the considered simulations (Figure 7). Model stations (hereafter ST)
448 chosen for the data analysis are shown in Figure 1.
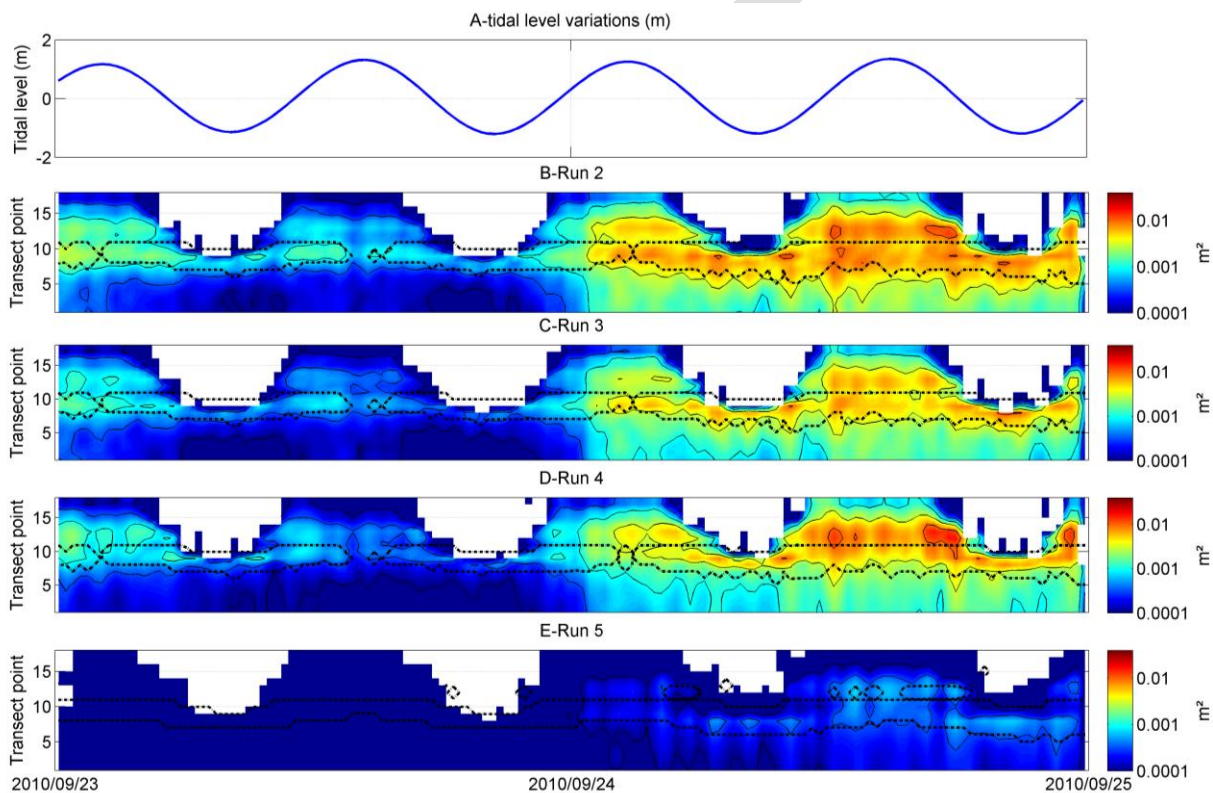
449

450 Figure 7.A) Time series of the tidal free surface elevation at ST2, and time series of the
451 simulated *IG wave* energy along the transect shown in Figure 1: B) Run2: with incoming bound
452 wave and wave forces activated everywhere, C) Run3: same as 2 without wave forces in the
453 surf-zone, D) Run4: no incoming bound-wave nor wave forces outside the surf-zone, E) Run5:
454 with incoming bound-wave and without wave groups. The locations of stations along the
455 selected transect are shown in Figure 1. The dashed lines delimit the surf-zone.

456 In general, energy levels at Run 2 and 4 were higher than at 3 and 5. In Run 2 the maximum
457 energy levels where 0.012 m^2, which is equivalent to $H_{m0,IG}$ of 0.45 m. In all simulations energy
458 increased from offshore to the ebb-tidal delta (ST 7-11), where maximum values were reached.
459 When water levels exceeded mean water levels two local maxima were observed. The first one
460 was located in the offshore edge of the ebb-tidal delta, between ST 8 and 10. The second was

15

461 located in the inlet mouth, between ST 12 and 14. During the rest of the tidal cycle only one
462 maximum, at the edge of the ebb-tidal delta, was observed. The location was tidally modulated,
463 closer to the inlet at high tide and more offshore at low tide. Energy was higher inside the surf-
464 zone for run 4 and conversely, slightly higher outside the surf-zone for Run 3. Run 5 was
465 designed to investigate the contribution of the incoming bound wave and its shoaling across the
466 domain without any further forcing mechanism (Figure 7E). The IG energy variance in Run 5
467 was one order of magnitude smaller than in the rest of the runs, which indicates that this
468 mechanism is not dominant, therefore it will not be further discussed.

469 Run 3 was designed to compute the contribution of the bound wave mechanism in IG wave
470 generation while Run 4 was designed to isolate the contribution of the breakpoint mechanism. In
471 order to better quantify the contribution of each mechanism, we also computed the ratio between
472 IG energy variance from Run 3 (resp. Run 4) normalized by the linear sum of the IG energy
473 variance from Run 3 and 4 (Figure 8B and 8C, respectively). Outside the surf-zone and up to the
474 middle of the surf-zone, the bound wave mechanism is responsible for 40 to 70 % of the IG
475 energy variance, while from the inner part of the surf-zone to the shoreline and the inlet mouth,
476 the breakpoint mechanism turns dominant at the lower stages of the tide and is responsible for 50
477 to 90% of the IG energy variance. During high-tide, the relevance of the breakpoint mechanism
478 decreases, which could be due to less intense wave breaking over the steepest part of the ebb-
479 shoal. This behavior would also explain the shapes of the observed time series of $H_{mo,IG}$
480 measurements, with two local maxima (one at flood and the other at ebb tide) and a local
481 minimum during high-tide.

482 In order to detect possible interactions between both mechanisms, we computed the linear sum of
483 the IG energy variance from Run 3 and 4 normalized by the IG energy variance of Run 2 (Figure
484 8D). All along the considered time series, the normalized sum is close or higher than 100%, with
485 local values reaching 200% along the shoreline. This behavior suggests that the bound-wave and
486 the breakpoint mechanisms acted in opposite ways and resulted on a reduction of $H_{m0,IG}$
487 compared to a situation where both mechanisms would act independently. Since the bound-wave
488 is out of phase with the wave envelope and the wave setup is in phase, the combination could
489 create a destructive interaction and result on a reduction of the amplitude of the observed IG
490 waves. In addition, Run 3 does not include wave forces inside the surf-zone and therefore the
491 mean wave setup is not accounted for. Additional tests with a simple 1D shoaling model (energy
492 flux conservation) suggest that considering wave setup could reduce IG wave energy by ~8 %.
493 Therefore, this effect could also contribute to explain departures from 100 % in Figure 8D.

494
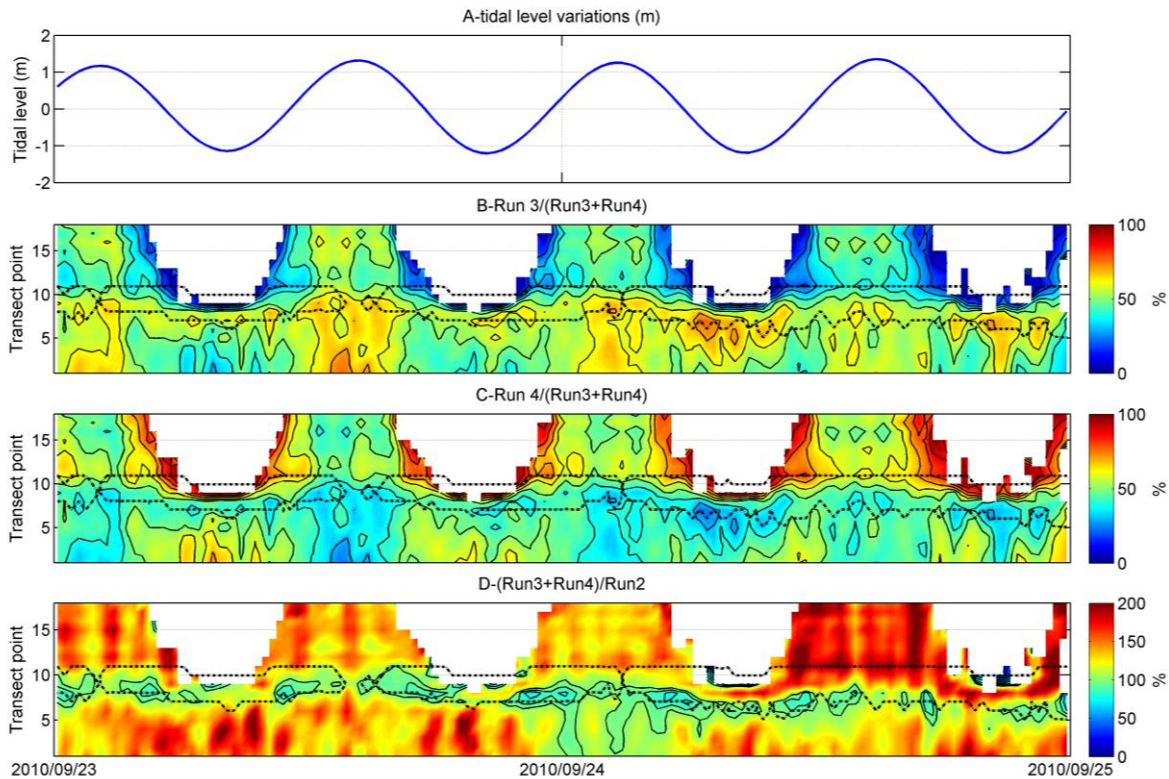
Figure8. A) Time series of the free-surface elevation due to tides in ST2. (B) Percentage of *IG energy variance* due to bound wave mechanism compared to breakpoint mechanism, C) Percentage of *energy variance* due to breakpoint mechanism compared to bound wave mechanism and D) Sum of energy variance of Run 3 and Run 4 normalized by Run 2, showing relevant interactions between both mechanisms.

### 5.3 IG wave propagation from the ebb-tidal delta to the inner lagoon

IG wave propagation from the ebb-tidal delta to the inner part of the lagoon is complex and highly dependent on the tidal phase. $H_{m0,IG}$ variation from the offshore to the inner part of the lagoon showed that, independently of the tidal phase, the maximum IG energy peak was obtained over the ebb-tidal delta (Figure7). This maximum was followed by a decrease of $H_{m0,IG}$ between ST 10 and 12. At the inlet throat (ST 13 and 14) a second local minimum was observed during the flood and high tide. During low and ebb tide a drastic decrease of $H_{m0,IG}$ was detected at ST 13, in the modeling results as in the observations.

To have a better understanding of how the tidal stage can affect the IG wave propagation, we computed the spatial distribution of $H_{m0,IG}$ at different tidal instants during the last tidal cycle (Figure 9), assuming stationary mean wave boundary conditions equivalent to those of September 24 at 9:00 AM ($H_{m0,G}$=1.55 m, T_p= 19.3 s and 264 degrees peak direction in nautical convention). $H_{mo,IG}$ was computed after splitting the modeled free-surface elevation into consecutive bursts of 30 minutes. To be consistent with this burst, currents were also averaged over 30 minute intervals.

516 Model results indicate that during maximum ebb and low tide, the maximum $H_{m0,IG}$ was
517 restricted to the terminal lobe, whereas during high tide and mid flood infragravity energy
518 propagated throughout the ebb-tidal delta. During mid ebb, IG wave energy reached the inlet
519 mouth but the energy did not propagate into the lagoon, it got blocked. Tidal currents at the inlet
520 were more intense than 1.8 m/s, reaching peak values of 2.5 m/s in water depths ranging from 1
521 to 1.5 m (Figure 4). As the water depth decreased parts of the ebb-tidal delta became dry. IG
522 waves were mainly generated in the terminal lobe, where most of the wave breaking occurred.
523
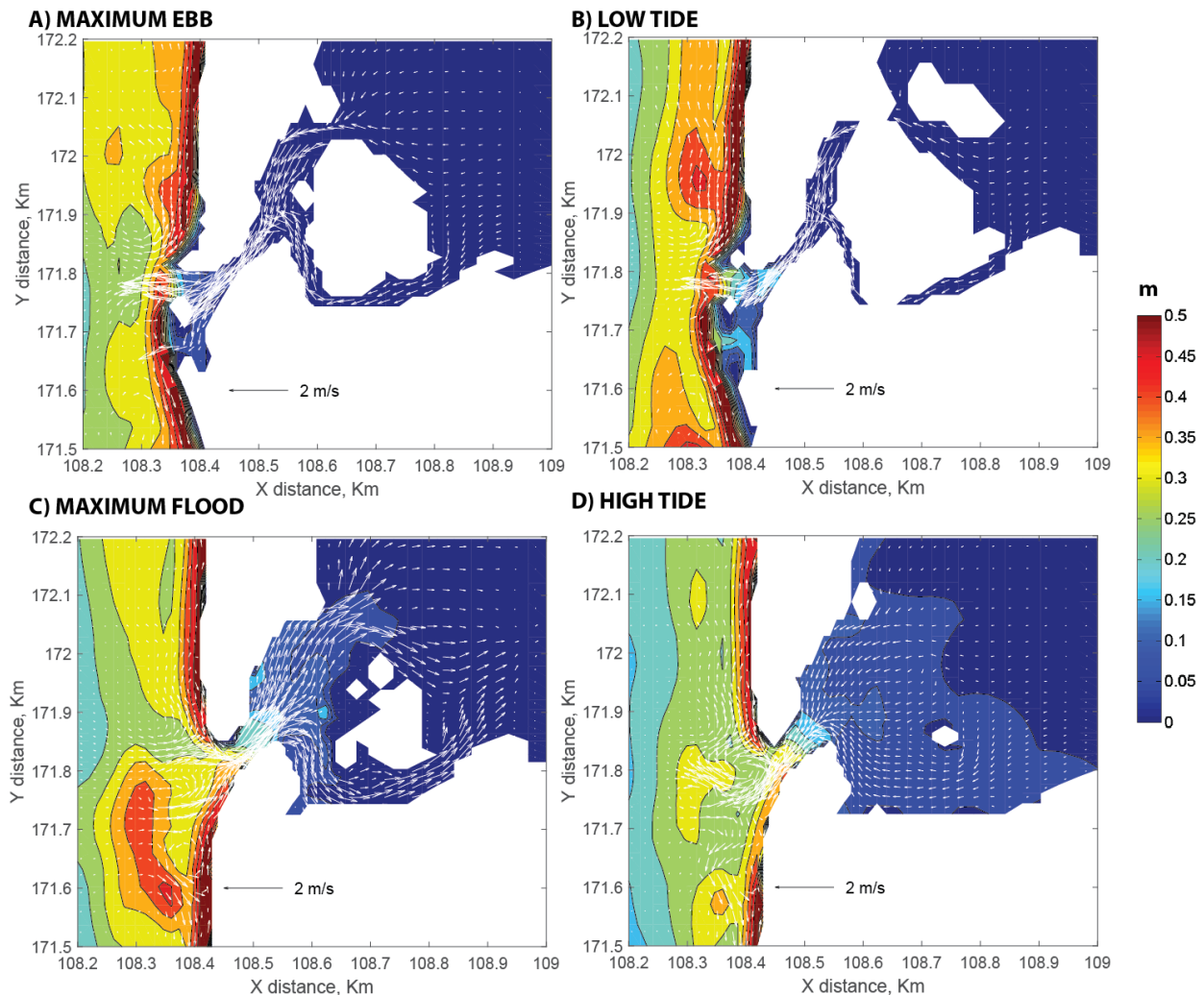
524
525 Figure9. Simulated $H_{m0,IG}$ distribution and depth-averaged current vectors during a)
526 maximum ebb, b) low-tide, c) maximum flood, and d) high-tide of the last tidal cycle.
527 Current vectors were averaged over the length of the burst (30 minutes). High tide and
528 low tide are defined in terms of maximum and minimum water levels inside the lagoon.
529

530 Gravity waves at inlets get blocked during the maximum ebb and they break at or before the
531 blocking point without being reflected, while losing considerable amounts of energy due to
532 current induced whitecapping (Chawla and Kirby, 2002). Similarly, IG waves could be blocked
533 at the inlet and this could explain the drastic energy damping observed during the mid-ebb and
534 low tide between PT1 and the inner stations, both in the measurements and in the model. Wave

535 blocking happens when the absolute wave group celerity falls to zero, in other words, when the
536 relative group celerity is equal to the opposing current speed:
537
538 $$C_{g,a} = C_{g,r} + U \cos \alpha = 0 \quad (6)$$
539
540 where $C_{g,a}$ and $C_{g,r}$ are the absolute and relative wave group celerities, respectively, U is the
541 vertically averaged current speed and α is the angle between waves and currents. When blocking
542 occurs, the wave energy cannot propagate against the current.
543
544 The linear wave dispersion relationship affected by the Doppler shift can be used to determine
545 the maximum period blocked by an opposing current with a given intensity:
546
547 $$\sigma^2 = \left(w_a - kU \cos \alpha \right)^2 = gk \tanh(kh) \quad (7)$$
548
549 Where σ is the intrinsic or relative frequency, w_a is the absolute frequency, U the magnitude of
550 the depth-averaged velocity, k is the wavenumber, g the gravitational acceleration and h is the
551 total water depth.
552
553 We used the linear dispersion relation to determine, based on the computed water levels and
554 current speeds, where and when gravity and IG wave blocking occurred. As shown in Figure 10
555 (panels a and b), weaker opposing current speeds are required to block shorter period waves
556 according to the linear dispersion relation. For 1 m water depth, current velocities larger than 2.4
557 m.s^{-1} are theoretically required to block waves of any frequencies while for 0.5 m water depth,
558 this value drops to 1.7 m.s^{-1}. IG wave blocking in the last tidal cycle got initiated at the inlet
559 mouth (Figure 10c), where tidal current speeds up to 2.5 m/s were modeled from mid-ebb to low
560 tide, with water depths varying from 1.5 to 1 m. Gravity-wave blocking was initiated earlier and
561 further offshore.
562

a) Wavelength according to the linear dispersion relation h=0.5 m

b) Wavelength according to the linear dispersion relation h=1.0 m

c) IG wave blocking location during the last tidal cycle
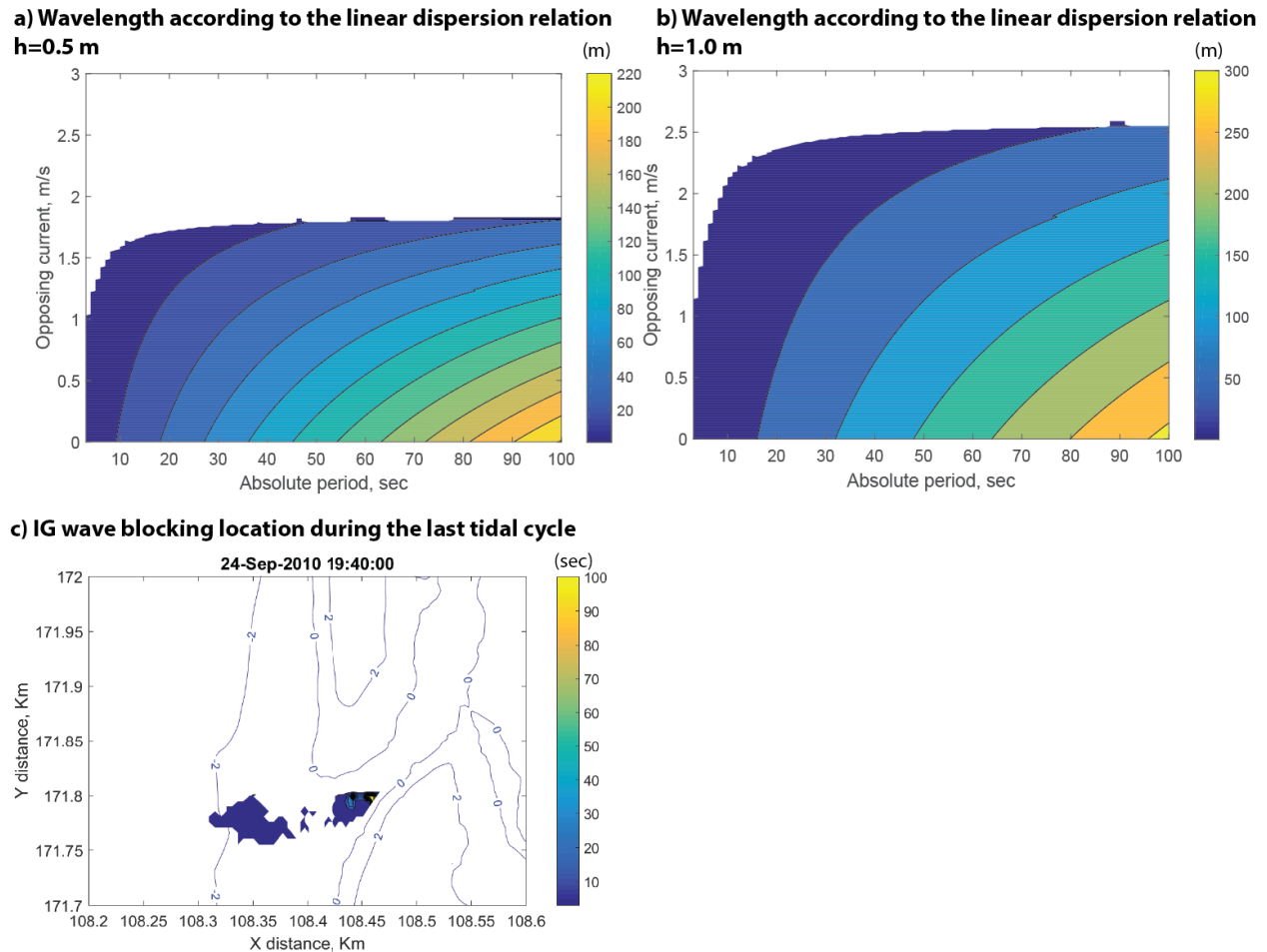
563
564 Figure 10. Contour map of the wave length (m) as a function of the opposing current
565 velocity given by the linear dispersion relation, a) for a water depth of 0.5 m and b) for a
566 water depth of 1 m. The white area indicates that there is no real solution and the
567 maximum period indicates the maximum period that is blocked; c) IG wave blocking
568 location computed with the linear-dispersion relation during tidal cycle 3 and bathymetric
569 contour lines in blue. The color indicates the maximum period (s) that is being blocked.
570
571 Measured gravity waves at PT2 and PT3 were blocked earlier (20 minutes in average) than the
572 infragravity band (Figures 3, 5 and 6), mainly because lower speed currents and/or larger water
573 depth are required to block lower period waves (Figure 10).
574

5.4 Possible impacts on sediment dynamics

576 The propagation of IG waves across the inlet induced current fluctuations that reached more than
577 50% of the tidal current intensity at PT2 during all the experiment, but especially in the third
578 tidal cycle (Figure 4). Although this behavior was reasonably reproduced by XBeach, a direct
579 comparison with the measured time series was not possible because the phase of the gravity
580 wave frequency components at the offshore boundary were unknown. Alternatively, the standard
581 deviation of current velocities were computed over 30 minute samples and compared. This
582 comparison revealed that XBeach was able to capture the temporal pattern of these low-

583 frequency fluctuations, although with a substantial underestimation of the peak, which occurred
584 during the maximum flood currents. Because sand fluxes depend non-linearly both on water
585 levels and currents, they may be affected by the presence of low-frequency fluctuations
586 associated with IG waves.

587 These low frequency fluctuations associated with IG waves would tend to promote sand fluxes,
588 but their blocking during a large part of the ebb would cause this process to be more active
589 during the flood. Over a tidal cycle, this process would tend to limit ebb-dominance in the main
590 channel and promote flood-dominance inside the lagoon. One should keep in mind that this
591 experiment was carried out under low to moderate energy waves and it can be expected that
592 under storm waves, larger IG waves would induce larger current fluctuations which could have a
593 determinant impact on the inlet sediment dynamics. In particular, this mechanism could
594 potentially contribute to the shoaling and closure of tidal inlets that occurs in winter along the
595 western coast of Portugal (Bertin et al., 2009; Dodet et al., 2013; Fortunato et al., 2014). Further
596 field measurements should be carried out under storms and under less energetic but more
597 frequent swell conditions, with a deployment specifically dedicated at measuring IG waves and
598 their subsequent dynamics.

599 **5 6. SUMMARY AND CONCLUSIONS**
600 Field measurements conducted at the Albufeira Lagoon Inlet revealed that IG waves developed
601 on the ebb-tidal delta and propagated inside the lagoon during flood and high tide, while they
602 were blocked during the ebb. The field experiment covered three tidal cycles, during spring tides.
603 Offshore significant wave height and the peak period increased due to the effect of a remote
604 storm that generated energetic swell conditions that impacted the study zone at the end of the
605 experiment. During the last tidal cycle, when the offshore waves were most energetic, $H_{mo,IG}$
606 values over 0.5 m were measured at the ebb-tidal delta. Inside the lagoon values up to 0.2 m
607 were measured.
608
609 The comparison between measurements and numerical simulations showed that IG wave
610 generation and propagation were fairly reproduced with XBeach. This fact indicates that,
611 although XBeach simplifies and neglects some physical processes that can affect both the
612 generation and the propagation of IG waves, the model captures the main processes. The analysis
613 of model results revealed that the two proposed IG wave generation mechanisms (the breaking
614 point variation or dynamic set-up and shoaling and release of the bound-wave) were relevant,
615 and contributed significantly to the IG wave generation. While the bound-wave shoaling was
616 dominant offshore the breaking area, wave breaking contribution was slightly higher from the
617 ebb-tidal delta to the inlet mouth. Model results also suggest that interactions between bound-
618 wave shoaling and the dynamic set-up, produced a reduction of IG energy levels within the surf-
619 zone.
620
621 IG waves were shown to be blocked during the ebb, due to strong counter tidal currents in
622 shallow water depths. IG wave blocking occurred later than the gravity-band blocking because
623 stronger opposing currents and shallower depths are needed to block longer period waves.
624
625 Field measurements and XBeach simulations demonstrated that, at least at this specific inlet, IG
626 wave generation, propagation, and dissipation mechanisms differed substantially from those
627 observed in beach environments. Due to steep bottom slopes at the terminal- lobe and gentle

628 slopes in the inner part of the ebb-tidal delta, the bound-wave shoaling and release and the
629 "dynamic" set-up mechanisms were both active during the analyzed period. Moreover, results
630 have shown another relevant difference with respect to the beach environments: while in beach
631 environments the IG wave energy is dissipated or reflected in the coast, in tidal inlets the energy
632 is partially transmitted to the inner part of the lagoon depending on the water levels and tidal
633 currents at the inlet.

634

635 Both measurements and model results showed that IG waves induced fluctuations in flood
636 currents inside the lagoon reaching temporarily 100 % of the low-pass filtered current
637 magnitudes (although the largest fluctuations were underestimated in the model). The fact that
638 these fluctuations occur mostly at flood and not at ebb because IG waves are blocked could
639 promote flood dominance in the lagoon. This mechanism could contribute the shoaling and
640 closure of tidal inlets, in combination to other wave-induced processes previously analyzed (e.g.
641 Bertin et al., 2009; Dodet et al., 2013). However, the field experiment presented in this study was
642 carried out under low to moderate wave energy and doesn't allow for a quantification of the
643 impact of IG waves on the inlet sediment dynamics. Additional field measurements designed to
644 measure infragravity wave propagation and transformation, the implications on the fluctuation of
645 currents and the subsequent impacts on sediment transport dynamics will have to be carried out
646 in such shallow inlets, under storm waves and mean wave conditions.

647

648 **ACKNOWLEDGEMENTS**

659

660 **APPENDIX A**

661 Considering that M_n and C_n are the measured data and the computed data, respectively, at N
662 discrete points, the model performance (skill, *S*) formula proposed by Wilmott (1981) is given
663 by:

664

$$S = 1 - \frac{\frac{1}{N} \sum_{n=1}^{N} |C_n - M_n|^2}{\sum_{n=1}^{N} \left(|C_n - \overline{M_n}| + |M_n - \overline{M_n}| \right)^2}$$

666

667 The overbar represents the mean value. This skill factor ranges from 0 (bad skill) to 1 (very good
668 skill).

669
670

672 **REFERENCES**
673 Arnaud, G., et X. Bertin (2014), Contribution du setup induit par les vagues dans la surcote
674   associée à la tempête klaus. XIII èmes Journées Nationales Génie Côtier _ Génie Civil, pp.
675   859_867.

676 Baldock, T. E. (2012), Dissipation of incident forced long waves in the surf zone—Implications
677   for the concept of "bound" wave release at short wave breaking, *Coastal Eng.*, 60, 276–285,
678   doi:10.1016/j.coastaleng.2011.11.002.

679 Baldock, T.E., O'Hare, T.J., Huntley, D.A., (2004), Long wave forcing on a barred beach,*J.*
680   *Fluid Mech.* 503, 321–343.

681 Baldock, T. E., and D. A. Huntley (2002), Long-wave forcing by the breaking of random gravity
682   waves on a beach, Proc. R. Soc. London, Ser. A, 458, 2177–2201.

683 Battjes, J. A., H. J. Bakkenes, T. T. Janssen, and A. R. van Dongeren (2004), Shoaling of
684   subharmonic gravity waves, J. Geophys. Res., 109, C02009, doi:10.1029/2003JC001863.

685 Bendat, J.S. and Piersol, A.G., 1971. Random Data: Analysis and Measurement Procedures.
686 John Wiley and Sons, New York, NY.
687
688 Bertin, X., A. B. Fortunato, and A. Oliveira, A., (2009), A modelling-based analysis of processes
689   driving wave-dominated inlets, *Cont. Shelf Res.*, 29, 819–834.

690 Bertin, X., Li, K., Roland, A., Bidlot, J.-R., (2015), The contribution of short-waves in storm
691   surges: two case studies in the Bay of Biscay,*Cont. Shelf Res.* 96, 1-15.

692 Bonneton, E. Barthelemy, F. Chazel, R. Cienfuegos, D. Lannes, F. Marche, M. Tissier,
693   (2011),Recent advances in Serre–Green Naghdi modelling for wave transformation, breaking
694   and runup processes,*Eur. J. Mech. B, Fluids*, 30, pp. 589–597

695 Booij, N., Ris, R.C. & Holthuijsen, L.H., (1999), A third-generation wave model for coastal
696   regions, Part I, Model description and validation, *J.Geoph.Research*, 104, C4, 7649-7666.

697 Chawla, A. and Kirby, J.T. (2002), Monochromatic and random wave breaking at blocking
698   points,*J. of Geophys. Res.* 107: doi: 10.1029/2001JC001042.

699 Chen, J.-L., T.-J. Hsu, F. Shi, B. Raubenheimer, and S. Elgar, 2015. Hydrodynamic and sediment
700   transport modeling of New River Inlet (NC) under the interaction of tides and waves, *J.*
701   *Geophys. Res.* Oceans, 120, doi:10.1002/2014JC010425.

702 Crawford, W., Ballu, V., Bertin, X. and Karpytchev, M., (2015), The sources from deep-ocean
703   infragravity waves in the North Atlantic Ocean, J. Geophys. Res. Oceans, 120, 5120–5133,
704   doi:10.1002/2014JC010657.

705 Daly, C., D. Roelvink, A. van Dongeren, J. van Thiel de Vries, R. McCall, (2012). Validation of
706   an advective-deterministic approach to short wave breaking in a surf-beat model, Coastal

707   Engineering, Vol 60, February 2012, 69-83, ISSN 0378-3839.

708 Dee D. P., S. M. Uppala, A. J. Simmons *et al.*(2011), The ERA-Interim reanalysis: configuration
709   and performance of the data assimilation system, *Q.J.R. Meteorol. Soc.*, 137(656), 553-597,
710   doi:10.1002/qj.v137.656.

711 Dodet, G., (2013), Morphodynamic modelling of a wave-dominated tidal inlet: the Albufeira
712   Lagoon, unpublished PhD Thesis, La Rochelle University, France, 207pp.

713 Dodet, G., Bertin, X., and Taborda, R., (2010), Wave climate variability in the North-East
714   Atlantic Ocean over the last six decades,*Ocean Modelling*, 31: 120-131.

715 Dodet, G., X. Bertin, N. Bruneau, A. B. Fortunato, A. Nahon, and A. Roland, (2013), Wave-
716   current interactions in a wave-dominated tidal inlet, *J. Geophys. Res. Oceans*, 118, 1587–
717   1605, doi: 10.1002/jgrc.20146.

718 Eldeberky, Y., (2015),Applicability of a Stochastic Model to Nonlinear Shoaling of Surface
719   Waves,*Coast. Eng. J.*, 57, 1550002 DOI: 10.1142/S0578563415500023.

720 Fortunato, A.B., Nahon, A., Dodet, G., Rita Pires, A., Conceição Freitas, M., Bruneau, N.,
721   Azevedo, A., Bertin, X., Benevides, P., Andrade, C. and Oliveira, A. (2014),Morphological
722   evolution of an ephemeral tidal inlet from opening to closure: The Albufeira inlet,
723   Portugal,*Cont. Shelf Res.* 73, 49-63.

724 Galappatti, R., and C. B. Vreugdenhil, (1985) A depth-integrated model for suspended sediment
725   transport, *J. Hydraul. Res.*, 23(4), 359– 377,.

726 Grant, W.D., Madsen, O.S., (1979), Combined wave and current interaction with a rough
727   bottom,*J. of Geophys. Res.* 84 (C4), 1797–1808.

728 Guza, R. T., E. B. Thornton, and R. A. Holman (1984), Swash on steep and shallow beaches, in
729   Proceedings of the Coastal Engineering Conference, 1984, edited by B. L. Edge, pp. 708–
730   723, Am. *Soc. of Civ. Eng.*, Reston, Va.

731 Hasselmann, K., (1962), On the non-linear transfer in a gravity spectrum, Part 1. General
732   theory,*J. Fluid Mech.*, 12, 481-500.

733 Herbers, T.H.C., Elgar, S., Guza, R.T, (1994), Infragravity-frequency (0.005–0.05 Hz)motions
734   on the shelf, part I, Forced waves,*J. Phys. Oceanogr.* 24, 917–927.

735 Herbers, T.H.C., Elgar, S., Guza, R.T, (1995), Generation and propagation of
736   infragravitywaves,*J. Geophys. Res.* 100, 24, 863–24, 872.

737 Kennedy, A., Chen, Q., Kirby, J., and Dalrymple, R. (2000),Boussinesq Modeling of Wave
738   Transformation, Breaking, and Runup.I: 1D,*J. Waterway, Port, Coastal, Ocean Eng.*, 126(1),
739   39–47.

740   List, J. H. (1992), A model for the generation of two-dimensional surfbeat, *J. Geophys. Res.*, 97,
741   5623– 5635.

742   Long, J. W., and H. T. Özkan-Haller (2009), Low-frequency characteristics of wave group–
743   forced vortices, *J. Geophys. Res.*, 114, C08004,doi:10.1029/2008JC004894.

744   Longuet-Higgins, M. S., and R. W. Stewart (1962), Radiation stress and mass transport in
745   gravity waves, with application to 'surf beats', *J. Fluid Mech.*, 13, 481–504.

746   Longuet-Higgins, M. S., and R. W. Stewart (1964), Radiation stresses in water waves: A
747   physical discussion, with applications, *Deep Sea Res.*, 11, 529–562.

748   Ma, G., F. Shi, J.T. Kirby (2012). Shock-capturing non-hydrostatic model for fully dispersive
749   surface wave processes, Ocean Modelling, Volumes 43-44, 2012, Pages 22-35.

750   Madsen, P. A., Sørensen, O. R., and Schäffer, H. A. (1997), Surf zone dynamics simulated by a
751   Boussinesq-type model. Part II: Surf beat andswash oscillations for wave groups and
752   irregular waves,*Coast. Eng.*, 32, 289–319.

753   Malhadas, M. S., Leitao, P. C., Silva, A., and Neves, R. (2009), Effect of coastal waves on sea
754   level in Óbidos Lagoon, Portugal, *Cont. Shelf Res.*, 19 9 , 1240–1250.

755   Masselink, G. (1995), Group bound long waves as a source of infragravity energy in the surf
756   zone, *Cont. Shelf Res.*, 15, 1525–1547.

757   Okihiro, M., Guza, R. T., (1996),Observations of Seiche Forcing and Amplification in Three
758   Small Harbours,*J. Waterw. Port Coast. Ocean Eng.* 122(5),232–238.

759   Olabarrieta, M., J. C. Warner, and N. Kumar, (2011), Wave-current interaction in Willapa Bay,
760   *J. Geophys. Res.*, 116, C12014, doi:10.1029/ 2011JC007387.

761   Olabarrieta, M., W. R. Geyer, and N. Kumar, (2014), The role of morphology and wave-current
762   interaction at tidal inlets: An idealized modeling analysis, *J. Geophys. Res. Oceans*, 119,
763   8818–8837, doi:10.1002/2014JC010191.

764   Orescanin, M., B. Raubenheimer, and S. Elgar, (2014), Observations of wave effects on inlet
765   circulation, *Cont. Shelf Res.*, 82, 37–42.

766   Pomeroy, A., R. Lowe, G. Symonds, A. Van Dongeren, and C. Moore (2012), The dynamics of
767   infragravity wave transformation over a fringing reef, *J. Geophys. Res.*, 117, C11022,
768   doi:10.1029/2012JC008310.

769   Reniers, A.J.H.M., Groenewegen, M.J., Ewans, K.C., Masterton, S., Stelling, G.S., Meek, J.,
770   (2010), Estimation of infragravity waves at intermediate water depth,*Coastal Eng.* 57, 52–61.

771   Reniers, A.J.H.M., MacMahan, J., Thornton, E.B., Stanton, T.P., (2006), Modelling infragravity
772   motions on a rip-channel beach,*Coast. Eng.* 53, 209–222.

773 Reniers, A.J.H.M., Thornton, E.B., Stanton, T.P., Roelvink, J.A., (2004), Vertical flow structure
774   during Sandy Duck: observations and modeling,*Coast. Eng.* 51, 237–260.

775 Rijnsdorp, D. P., G. Ruessink, and M. Zijlema (2015), Infragravity-wave dynamics in a barred
776   coastal region, a numerical study, J. Geophys. Res. Oceans, 120, 4068-4089,
777   doi:10.1002/2014JC010450

778 Roelvink J.A., Reniers A.J.H.M., Van Dongeren A.R., Van Thiel de Vries J.S.M., McCall R.T.,
779   Lescinski J., (2009), Modeling storm impacts on beaches, dunes and barrier islands, *Coast.*
780   *Eng.*, 56 (11-12), 1133-1152, doi: DOI: 10.1016/j.coastaleng.2009.08.006.

781 Ruju, A., Lara, J., Losada, I., 2012. Radiation stress and low-frequency energy balance within
782   the surf zone: A numerical approach, Coastal Engineering 68, 44-55.

783 Schäffer H.A, (1993), Infragravity waves induced by short wave groups,*J. Fluid Mech.* 247,
784   551–588.

785 Sénéchal, N., P. Bonneton, and H. Dupuis (2001), Field observations of irregular wave
786   transformation in the surf zone, in *Coastal Dynamics* '01,pp. 62– 71, Am. Soc. of Civ. Eng.,
787   Reston, Va.

788   Sheremet, A., J.R. Davis,M.Tian,J.L.Hanson,K.K.Hathaway, 2016.TRIADS:A phase-resolving
789   model for nonlinear shoaling of directional wave spectra. Ocean Modelling 99, 60–74.

790 Siegle, E., D. A. Huntley, and M. A. Davidson, (2004), Physical controls on the dynamics of
791   inlet sandbar systems, *Ocean Dyn.*, 54(3–4), 360–373.

792 Soulsby, R. (1997), Dynamics of marine sands, a manual for practical applications,. Thomas
793   Telford, ISBN 0-7277-2584X, H.R. Wallingford, England, 249 pp.

794 Symonds, G., Huntley, D.A, Bowen, A.J, (1982), Two-dimensional surf beat: long wave
795   generation by a time-varying breakpoint,*J. Geophys. Res.* 87, 492–498.

796 Tolman H. L. (2009), User manual and system documentation of WAVEWATCH III TM
797   version 3.14, Technical note, MMAB Contribution, 276, 220.

798 Torres-Freyermuth, A., J.L. Lara, I.J. Losada, (2010), Numerical modelling of short-and long-
799   wave transformation on a barred beach, *Coast. Eng.*, 57 (2010), pp. 317–330.

800 Uchiyama, Y., and J. C. McWilliams (2008), Infragravity waves in the deep ocean: Generation,
801   propagation, and seismichum excitation, *J. Geophys. Res.*, 113, C07029,
802   doi:10.1029/2007JC004562.

803 van Dongeren, A., J. Battjes, T. Janssen, J. van Noorloos, K. Steenhauer, G. Steenbergen, and A.
804   Reniers (2007), Shoalingand shoreline dissipation of low-frequency waves, *J. Geophys. Res.*,
805   112, C02011, doi:10.1029/2006JC003701.

806   Wargula, A., B. Raubenheimer, and S. Elgar (2014), Wave-driven along-channel subtidal flows
807   in a well-mixed ocean inlet, *J. Geophys. Res.* Oceans, 119, 2987–3001,
808   doi:10.1002/2014JC009839.

809   Willmott, C. J. (1981), On validation of models, Phys. Geogr., 2, 184– 194.

810   Zijlema, M., Stelling, G. and Smit, P., (2011), SWASH: An operational public domain code for
811   simulating wave fields and rapidly varied flows in coastal waters, *Coast. Engng.*, 58, 992-
812   1012.